Research article

Pulse electrodeposition of CuSbS$_2$ thin films: Role of Cu/Sb precursor ratio on the phase formation and its performance as photocathode for hydrogen evolution[§][☆]

R.G. Avilez García [a,b], Andrea Cerdán-Pasarán [c], J.P. Enríquez [b], N.R. Mathews [a,*]

[a] *Instituto de Energías Renovables, Universidad Nacional Autónoma de México, Temixco, Morelos 62580, Mexico*
[b] *Instituto de Investigación e Innovación en Energías Renovables, Universidad de Ciencias y Artes de Chiapas, Libramiento Norte # 1150 Lajas Maciel, C.P. 29039 Tuxtla Gutiérrez, Chiapas, Mexico*
[c] *Universidad Autónoma de Nuevo León, Facultad de Ciencias Químicas, Av. Universidad, Cd. Universitaria, San Nicolás de los Garza, Nuevo León C. P. 66455, Mexico*

ARTICLE INFO

ABSTRACT

In this paper, we outline the development of stoichiometric chalcostibite, CuSbS$_2$ thin films, from a single bath by pulse electrodeposition for its application as a photocathode in photoelectrochemical cells (PEC). The Cu/Sb precursor molar ratio of the deposition bath was varied to obtain stoichiometric CuSbS$_2$ thin films. The optimized deposition and dissolution potentials were -0.72 V and -0.1 V vs saturated calomel electrode, respectively. The formation of CuSbS$_2$ was analyzed using different characterization tools. X-ray diffraction and Raman results showed the formation of the pure chalcostibite phase from a precursor bath with molar ratio Cu/Sb = 0.41. The heterostructure CuSbS$_2$/CdS/Pt was tested as a photocathode in the PEC. The energy positions of the conduction and valence bands were estimated from the Mott Schottky plots. The conduction band and valence band offset of CuSbS$_2$/CdS heterojunction were 0.1 eV and 1.04 eV, respectively. The electric field created in the junction reduced the recombination of the electron/hole pairs and improved charge transfer in the interface. The heterostructure CuSbS$_2$/CdS/Pt demonstrated an improved photocurrent density of 3.4 mA cm^{-2} at 0 V vs reversible hydrogen electrode. The PEC efficiency obtained from the CuSbS$_2$/CdS heterojunction was 0.56 %. Therefore, we demonstrated the feasibility of an inexpensive technique like electrodeposition for the development of an efficient earth-abundant photocathode.

1. Introduction

The shift towards clean energy technologies is an important criterion to control the use of fossil fuels and thus global environmental pollution. Photovoltaic (PV) technology and photoelectrochemical cells (PEC) offer clean and sustainable energy by converting sunlight into electricity. PV technology is readily available in the market, reaching efficiencies for monocrystalline and polycrystalline Si-based solar cells up to 26.3 % and 24.58 %, respectively, in the lab scale [1,2]. They are followed by thin-film solar cells such as CIGS and CdTe with efficiencies of 22.6 % and 22.1 %, respectively [3,4]. The production of storable hydrogen using photoelectrochemical

Table 1

Reports where CuSbS$_2$ tested previously as a photocathode. E$_{RHE}$: electrode potential vs reversible hydrogen electrode (RHE). E$_{SCE}$: electrode potential vs saturated calomel electrode (SCE).

Photocathode	Current density	Reference
CuSbS$_2$/CdS/Pt	4.20 mA cm^{-2} at 0 E$_{RHE}$	[16]
FeZn$_{0.2}$Cd$_{0.8}$S/CuSbS$_2$	0.31 mA cm^{-2} at 0.9 E$_{RHE}$	[22]
CuSbS$_2$ microspheres	0.06 mA cm^{-2} at 1.23 E$_{RHE}$	[23]
TiO$_2$/graphene/CuSbS$_2$	5.50 mA cm^{-2} at 0.4 E$_{SCE}$	[24]

water splitting is an alternative for clean energy. The PEC concept was first reported using n-type TiO$_2$ by Honda and Fujishima [5]. To accomplish commercial level PEC, stable, efficient, and low-cost photoelectrodes must be developed. In the past decade, different metal oxide/sulfide materials such as TiO$_2$ [6,7], ZnO [8], α-Fe$_2$O$_3$ [9], BiVO$_4$ [10], CdS [11], CuIn$_{1-x}$Ga$_x$(SSe)$_2$ [12], Cu$_2$ZnSnS$_4$ [13] have been studied.

Among the different environmentally friendly semiconductor materials under consideration as photoelectrodes the ternary chalcogenide semiconductors based on copper, Cu$_y$MX$_z$ (M = Sn, Sb, Bi and X = S, Se, Te), have great prospects [14–17]. The Cu–Sb–S system is particularly interesting because of their conductivity type, abundant raw materials, and low toxicity. The four relevant phases of this system are CuSbS$_2$, Cu$_3$SbS$_4$, Cu$_{12}$Sb$_4$S$_{13}$, and Cu$_3$SbS$_3$. Among them, CuSbS$_2$ (CAS) has an energy gap of 1.35–1.5 eV suitable for a single junction solar cell, a high absorption coefficient ($>10^4$ cm^{-1}) in the visible region, and adequate electrical properties such as hole mobility (49 cm^2 (Vs)$^{-1}$) and hole concentration 10^{16}- 10^{18} cm^{-1} [18]. Furthermore, these materials have a relatively low melting point, ~551 °C, indicating possible crystallization at lower temperatures.

CuSbS$_2$ thin films developed by a variety of techniques have been incorporated as light-absorbing layers in the solar cell structure. An efficiency (η) of 3.22 % was achieved for the Mo/CuSbS$_2$/CdS/i-ZnO/n-ZnO/Al structure and 2.48 % for the ITO/CdS/Ag:CuSbS$_2$/ Au structure, where the CuSbS$_2$ layers were deposited by spin coating and spray pyrolysis, respectively [19,20]. Seger et al., through computational modeling, have shown the potential of CuSbS$_2$ as a photocathode [21]. Furthermore, CuSbS$_2$ thin films have been successfully reported as photocathodes for the hydrogen evolution reaction (HER). The highest yield was 4.2 mA cm^{-2} at 0 E$_{RHE}$ for the CuSbS$_2$ photocathode processed by the Cu and Sb sequentially electrodeposited, followed by the sulfurization with H$_2$S flow [16]. Table 1 summarizes some important works on CuSbS$_2$ as photocathodes.

Although several methods have been reported for the development of CuSbS$_2$ thin films, due to the high possibility of the formation of binary (Cu$_2$S, Sb$_2$S$_3$) and ternary (Cu$_{12}$Sb$_4$S$_{13}$, Cu$_3$SbS$_4$, Cu$_3$SbS$_3$) impurities, its formation as a stoichiometric phase remains a challenge. Physical and chemical methods for the development of CuSbS$_2$ thin films include sputtering [25], thermal evaporation [26], chemical bath deposition [27], sulfurization of electrodeposited metal stacks [28], spray pyrolysis [29], solution method [30], electrodeposition [31], etc. Vacuum-based routes are more expensive, so the non-vacuum methods such as electrodeposition and solution methods are more appropriate to reduce the cost of cell manufacturing. The feasibility of the electrodeposition technique has been demonstrated from the solar conversion efficiencies of CIGS (15.4 %) and Cu$_2$ZnSnS$_4$ (3.2 %) [32,33]. By this approach, uniform films with precise compositions can easily be obtained by changing deposition conditions such as bath composition, temperature, and deposition potential. Deposition of various semiconductors employing constant current or potential has been widely reported. In the pulsed electrodeposition method, pulses of currents or potentials are applied, offering significant control over the composition, morphology, and uniformity of the films [34]. To our best knowledge, a single step pulse electrodeposition of CuSbS$_2$ thin films from aqueous solutions and the role of Cu/Sb precursor ratio on the stoichiometry, physical and chemical properties is not reported. There are some studies on the role of Cu/Sb ratio of two-stage processed CuSbS2 thin films by chemical and evaporation methods [35,36].

In this work, we outline the one step electrodeposition of CuSbS$_2$ thin films on Fluorine doped SnO$_2$ (FTO) from a single bath containing SbCl$_3$, CuCl$_2$, and Na$_2$S$_2$O$_3$. Cyclic voltammetry was used as the technique to understand the electrochemical reactions involved in the formation of CuSbS$_2$. The metal precursor molar concentration, the Cu/Sb ratio, was optimized to obtain stoichiometric CuSbS$_2$ phase. The physicochemical properties of the films were effectively discussed using the results obtained from structural, morphological, and spectroscopic evaluation. The energy band alignment of CuSbS$_2$/CdS layers constructed from the band edges estimated from the Mott Schottky plots revealed a type II structure of the interface which promotes charge separation. The heterostructure CuSbS$_2$/CdS/Pt was developed, and we observed that the buffer layer CdS significantly improved the photocurrent and had a nominal dark current over a broad range of applied potentials. The CuSbS$_2$/CdS/Pt demonstrated a photocurrent density of 3.4 mA cm^{-2} at 0 V RHE, which is close to that reported for CuSbS$_2$ photocathodes. Therefore, we demonstrated the feasibility of electrodeposition for the development of earth-abundant photocathodes such as CuSbS$_2$ and its application in the cost-effective hydrogen evolution.

2. Experimental section

2.1. Cyclic voltammetry

Cyclic voltammetry (CV) studies were carried out to evaluate the redox reaction mechanisms of the electroactive species involved in the formation of CuSbS$_2$. The CV was done in an electrochemical cell with FTO, saturated calomel electrode (SCE) and platinum as working, reference and counter electrodes, respectively. Fig. 1 a-c shows the CV performed in separate solutions containing Cu^{2+}, Sb^{3+} and S$_2$O$_3^{2-}$, respectively. The potentials given in the CV study are with reference to SCE. The scan speed of the sweep was 10 mV/s. In
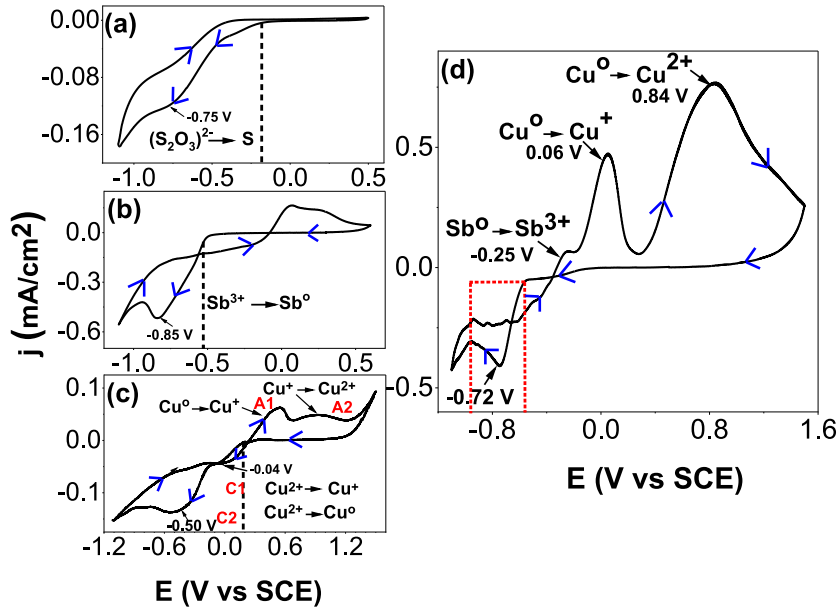
Fig. 1. Cyclic voltammetry in precursor solutions a) 18 mM Na$_2$S$_2$O$_3$, b) 1.3 mM SbCl$_3$, c) 0.5 mM CuCl$_2$ and d) mixed electrolyte containing ions of copper, antimony, and sulfur precursors on the FTO substrate. The scan speed was 10 mV/s.

the CV corresponding to sodium thiosulfate (18 mM Na$_2$S$_2$O$_3$) solution of pH = 5, the current was negligible till −0.07 V and then it started to increase showing a cathodic peak at −0.75 V (Fig. 1a). The thiosulfate ion has a structure similar to that of sulfate (-SO$_4$)$^{2-}$. To form thiosulfate ion, one of the oxygen atoms in the (-SO$_4$)$^{2-}$ is replaced by a sulfur atom and hence, the chemical environment of both the sulfur atoms are different. The (S–SO$_3$)$^{2-}$ has a sulfur atom as (SO$_3$)$^{2-}$ group, where the sulfur atom is bonded to 3 oxygen atoms and has a nominal + 6 oxidation state. The other sulfur atom is attached to the sulfur atom of the (SO$_3$)$^{2-}$ group and has an oxidation state of −2. The (-S$_2$O$_3$)$^{2-}$ groups have excellent reducing and complexing capacity towards metal ions [37]. The possible reactions involved in the increment of the cathodic current are given in eqs. (1)–(5). In an acidic medium, (-S$_2$O$_3$)$^{2-}$ can undergo a disproportionate reaction forming elemental sulfur, which can be further reduced to S^{2-}.

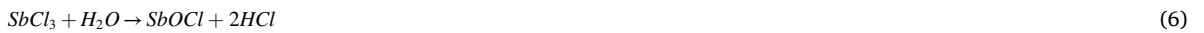$$(S_2O_3)^{2-} \xrightarrow{H^+} S + (SO_3)^{2-} \tag{1}$$

Both S and SO$_3$$^{2-}$ can be reduced to S^{2-} according to the equations given below

$$(SO_3)^{2-} + 4e^- + 6H^+ \rightarrow S + 3H_2O \tag{2}$$

$$S + 2H^+ + 2e^- \rightarrow H_2S \tag{3}$$

At the same time (S$_2$O$_3$)$^{2-}$ can undergo direct reduction forming S or S^{2-}

$$(S_2O_3)^{2-} + 6H^+ + 4e^- \rightarrow 2S + 3H_2O \tag{4}$$
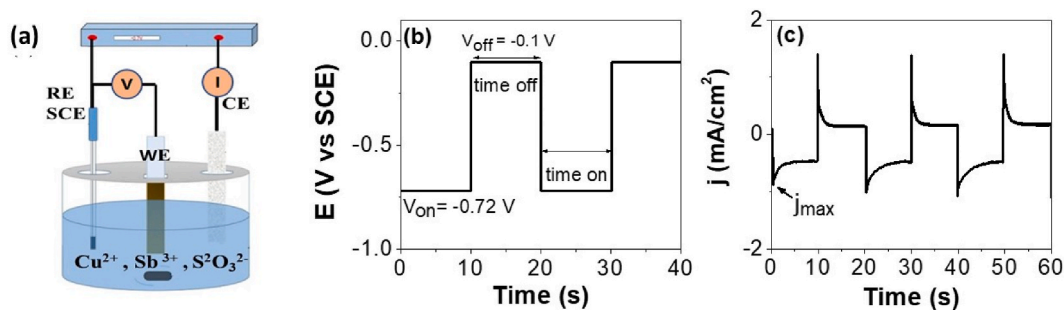
$$(S_2O_3)^{2-} + 6H^+ + 8e^- \rightarrow 2S^{2-} + 3H_2O \tag{5}$$

The CV done in the SbCl$_3$ solution (1.3 mM) of pH = 2 showed an increase of current ∼ −0.51 V and a cathodic peak at −0.85 V related to the Sb metal deposition (Fig. 1b). In aqueous solution, SbCl$_3$ forms SbOCl and is reduced to Sb by cathodic polarization (eq. (6) and (7)). At potentials < −1.0 V the hydrogen evolution reaction takes place, which is out of the scope of this experiment. The suitable potential for the deposition Sb is in range of −0.51 and −0.85 V. The reactions involved are shown below:

$$SbCl_3 + H_2O \rightarrow SbOCl + 2HCl \tag{6}$$

$$SbO^+ + 2H^+ + 3e^- \rightarrow Sb + H_2O \tag{7}$$

During the forward scan in the CuCl$_2$ solution (0.5 mM, pH = 3), cathodic current increased from ∼ +0.18 V with a small peak at −0.04 V followed by a strong cathodic peak at −0.50 V vs. SCE. The peak at −0.04 V (C1) corresponds to the reduction of Cu^{2+} to Cu$^+$ (eq. (8)) and at −0.50 V (C2) is the formation of Cu^o, eq. (9) (Fig. 1c). In the inverted sweep, two peaks (A1 and A2) corresponding to the oxidation reactions were observed.

$$Cu^{2+} + e^- \rightarrow Cu^+ \tag{8}$$

Fig. 2. Schematic representations of (a) the three-electrode set up employed for pulsed electrodeposition of CAS thin films, (b) potentials utilized during pulsed electrodeposition, (c) current profile during the first few cycles of the pulsed bias during electrodeposition, $V_{on} = -0.72$ V and V_{off} -0.1 V_{SCE}.

$$Cu^{2+} + 2e^- \rightarrow Cu^o \qquad (9)$$

Fig. 1d shows the CV measurement from a solution containing ions of copper, antimony, and sulfur precursors over a wide range of potentials from -1 to $+1.5$ V vs. SCE. The pH of the solution was ~ 2.8. The sharp rise in the current after -0.5 V indicates the possible co-electrodeposition of copper, antimony, and sulfur. The region where the three elements can possibly be co-electrodeposited is shown by the red dotted square. In the reverse scan, the oxidation peaks corresponding to the dissolution of Sb to Sb^{3+} (-0.25 V), Cu to Cu^+ (0.06 V), and Cu^{2+} (0.84 V) are clearly seen (Fig. 1d).

The possible final reactions during the formation of $CuSbS_2$ are given below (eqs. (10) and (11))

$$Cu^{2+} + Sb^{3+} + 2S + 5e^- \rightarrow CuSbS_2 \qquad (10)$$

$$Cu^{2+} + Sb^{3+} + 2S^{2-} + 1e^- \rightarrow CuSbS_2 \qquad (11)$$

The corresponding Nernst equations of the main electrochemical reactions (eqs. (4), (7) and (9)) at the cathode during the formation of $CuSbS_2$ are given below (eq.(12)–(14)).

$$E\left((S_2O_3)^{2-} \Big/ S\right) = E^o\left((S_2O_3)^{2-} / S\right) + \frac{RT}{4F} \ln\left[(S_2O_3)^{2-}\right][H^+]^6 \qquad (12)$$

$$E\left(SbO^+ / Sb^0\right) = E^o\left(SbO^+ / Sb^0\right) + \frac{RT}{3F} \ln [SbO^+][H^+]^2 \qquad (13)$$

$$E\left(Cu^{2+} / Cu^0\right) = E^o\left(Cu^{2+} / Cu^0\right) + \frac{RT}{2F} \ln\left[Cu^{2+}\right] \qquad (14)$$

The standard reduction potentials, $E^o(S/S^{2-})$, $E^o(S_2O_3{}^{2-}/S^{2-})$, $E^o(SbO^+/Sb^0)$ and $E^o(Cu^{2+}/Cu^0)$ are -0.48 V, -0.006 V, 0.208 V, and 0.34 V, respectively [38,39]. From CV measurements, we could identify a potential range where the elements could be co-electrodeposited.

2.2. Development of films

The deposition of CAS thin films was done in electrochemical cell identical to that described in CV studies, sec 2.1 (Fig. 2a). The technique used was pulse electrodeposition: applied deposition potential ($V_{on} = -0.72$ V vs SCE; 10 s) and dissolution potential (V_{off} $= -0.1$ V vs SCE; 10 s) at 50 % duty cycle (duty cycle $= \frac{time_{on}}{time_{on}+time_{off}}x100$) (Fig. 2b). The potentials were selected based on the CV studies (sec 2.1). A spontaneous increase in negative current was observed during V_{on}, reaching a maximum current (J_{max}) and then gradually decreasing (Fig. 2c). The observed decrease in current is due to the depletion of ions near the electrode surface during V_{on}. The V_{off} allows time for the redistribution of the precursor ions and the recovery of the homogeneity of the electrolyte for the next V_{on}. Also, during V_{off} the weakly deposited CAS re-dissolve resulting in the formation of uniform and adherent films. This process allows constant rate of deposition. During a deposition at constant applied potential, the redistribution process does not occur, and therefore the rate of deposition will be slow.

For the deposition of the films, the substrates were cleaned with soap and deionized water in an ultrasonic bath for 10 min, followed by an ethanol rinse. The reagents used were $CuCl_2$, $SbCl_3$, and $Na_2S_2O_3$ as Cu, Sb and S precursors. The bath for the deposition of the CAS films was prepared as follows: First, 25 mg of $SbCl_3$ was dissolved in 20 mL of acetone to which 50 mL of deionized water was added. To this solution, 300 mg of $Na_2S_2O_3$ was added and stirred for 20 min. Finally, 7 mg of $CuCl_2$ was added with constant stirring. The resultant was a clear yellowish-brown solution. The image of the final solution is shown in the supplementary section (Fig. S1). The thiosulfate acts as precursor for S as well as the complexing agent. The CAS thin films were deposited from baths of different Cu/Sb precursor molar ratios. For this, the concentration of the $SbCl_3$ in the bath was varied, while keeping the concentration of both $CuCl_2$
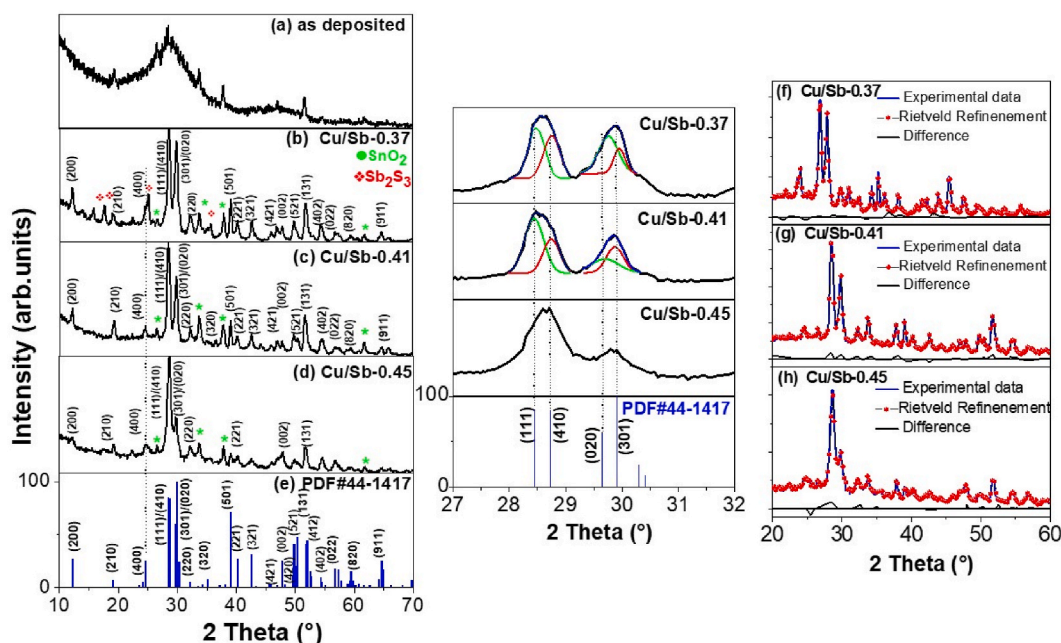
Fig. 3. (a–d) X-ray diffractogram of the CAS thin films pulse electrodeposited from baths with different precursor molar ratios. The Cu/Sb precursor molar ratios used for deposition were 0.37, 0.41, 0.45. In the middle, the XRD pattern zoom in 2-theta range 28–30°. (e) The reference pattern of orthorhombic $CuSbS_2$ (PDF#44–1417). (f–g) The Rietveld refinements performed on the XRD of the CAS films, the experimental data are solid blue lines and Rietveld refinement data are the red dots. The difference plot between the actual data and the Rietveld results is shown at the bottom (solid black line). (For interpretation of the references to colour in this figure legend, the reader is referred to the Web version of this article.)

and $Na_2S_2O_3$ fixed. The bath composition was 1.3–1.60 mM $SbCl_3$, 0.5 mM $CuCl_2$, and 18 mM $Na_2S_2O_3$. The temperature of the bath was maintained at 25 ± 2 °C and nitrogen was bubbled throughout the experiment to prevent any oxide formation. The pH of the solution was ∼2.8. The precursor molar ratios (Cu/Sb) investigated were 0.37, 0.41, 0.45. Based on the composition of the bath from which the films were deposited, they were labeled as Cu/Sb-0.37, Cu/Sb-0.41, Cu/Sb-0.45. The CAS films deposited were amorphous and a two-stage heat treatment was carried out for crystallization. Initially at 250 °C for 10 min, followed by 300 °C for half an hour in nitrogen and sulfur environment. 5 mg of elemental sulfur was used during each annealing process. The details are given in supplementary section (Fig. S2). The films were adherent and uniform. The thicknesses were obtained using a surface profilometer and were ∼500 nm. This was further confirmed from the cross-sectional images of the films (sec 3.2, Fig. 6).

2.3. Characterization techniques

X-ray diffraction (XRD) measurements were done with a Rigaku Ultima IV X-ray diffractometer (CuKα; wavelength (λ) = 0.154 nm) for 2 theta = 10° to 70° at a scan speed of 1°/min using grazing incidence (δ) of 0.5°. The grazing angle of 0.5° was selected to minimize the intensity of the substrate peaks. The sampling depth of the XRD analysis was 110 nm. The phase purity of the samples was further confirmed by Raman spectra recorded using an iHR550 Horiba-Jobin Yvon spectrophotometer. The samples were irradiated with a Helium–Neon laser of λ 632 nm. The morphological studies were done using an atomic force microscopy (AFM DI-Veeco Nanoscope IV system) and scanning electron microscope (SEM Hitachi SU1510). The elemental composition of the CAS films was analyzed using the energy-dispersive X-ray spectrometer (EDS) attached to the SEM. The chemical oxidation states of the elements were determined using an X-ray photoelectron spectroscopy (XPS Thermo Scientific K-alfa). The optical studies were done from the transmittance and the reflectance measurements using the UV–Vis spectrophotometer (UV- Shimadzu 3100 PC). The photo response of the CAS films was obtained in a sandwich arrangement with one contact from a carbon electrode of 0.15 cm^2 drawn on the film surface and the other contact from the FTO surface. The samples were illuminated from the FTO side and the dark and light currents were obtained under a constant applied voltage of 0.01 V. The schematic of the sandwich configuration is given in the inset of Fig. 8d.

2.4. Photoelectrochemical measurements

The photoelectrochemical characterization was performed in a three-electrode configuration, with the CAS films as the working electrode, SCE as the reference electrode, and Pt wire as the counter electrode. The photocathode was made by cutting the sample into 1×1 cm to obtain a surface area of 1 cm^2. The electrolyte used was 0.01 M H_2SO_4. The H_2SO_4 was added to improve the conductivity of the solution. The results of the photoelectrochemical studies are given with respect to reversible hydrogen electrode (RHE). The potentials in this work were measured with SCE and were converted to RHE based on the Nernst equation: $E_{RHE} = E_{SCE} + 0.059pH +$

Table 2

Crystal size, lattice parameters, volume cell, strain, dislocation density, and preferential orientation of the electrodeposited CAS thin films.

Sample	Molar ratio Cu/Sb	Crystal size (nm)	Lattice parameters (nm)			Volume cell (Å3)	σ	Dislocation density, δ (10-3 nm-2)	Strain 10^{-4}
			a	b	c				
Cu/Sb-0.37	0.37	16 ± 1	0.596	0.385	1.436	329.50	0.258	6.1	3.9
Cu/Sb-0.41	0.41	19 ± 2	0.599	0.379	1.464	332.35	0.306	5.2	2.7
Cu/Sb-0.45	0.45	15 ± 2	0.599	0.382	1.434	328.12	0.190	6.2	4.4

E^o_{SCE} where E_{RHE} is the electrode potential vs RHE, E_{SCE} and E^o_{SCE} are the applied and standard potentials with respect to SCE [40,41]. The chronoamperometric measurements (*i-t*) were done under chopped illumination (on/off cycles of 5 s) with an illumination intensity 100 mW cm^{-2} and an applied electrode potential of 0 V vs RHE. This figure is shown as the graphical abstract. The linear sweep (*i-v*) voltammetry was done at a scan rate of 10 mV/s under the same illumination source mentioned above. Electrochemical impedance spectroscopy (EIS) was done at open-circuit conditions with an AC amplitude of 15 mV over a frequency range of 0.001–1 KHz.

3. Results and discussion

3.1. Structural analysis

The structural evaluation of the films was done using XRD and Raman analysis. Fig. 3 shows the X-ray diffractograms of the CAS thin films obtained from the deposition baths with different Cu/Sb precursor molar ratios. Regardless of the bath composition, the CAS thin films deposited were not crystalline and the peaks of the FTO were only seen (PDF 41–1445) (Fig. 3a). After thermal treatment, the films became polycrystalline. Fig. 3b displays the XRD patterns of the CAS thin films deposited from a bath of Cu/Sb precursor molar ratio 0.37. The main peaks corresponding to CuSbS$_2$ can be seen, nevertheless, the presence of Sb$_2$S$_3$ binary phase is noticeable. The peaks of Sb$_2$S$_3$ are marked with "*" and are located at 2 theta values 15.58°, 17.64°, 25° and 35.59°. As the presence of Sb$_2$S$_3$ binary phase was clear from the XRD results, the concentration of SbCl$_3$ was reduced in the precursor solution. The film Cu/Sb-0.41 showed planes (200), (210), (111)/(410), (020)/(301), (501), (221), and (002) at 2 theta values 12.26, 19.30, 28.47/28.74, 29.71/29.88, 39.09, 40.12 y 47.86°, respectively (Fig. 3c). These are typical peaks of orthorhombic, chalcostibite CuSbS$_2$ phase (PDF#44–1417) and coincide well with the reports [42]. Peaks of impurity phases were not seen. The peaks at 2 theta values between 28 and 30° were analyzed in detail and are presented in the middle panel of Fig. 3. The planes (111)/(410) and (020)/(301) are very close and it was difficult to properly identify them. Hence a deconvolution of the XRD peaks of Cu/Sb-0.37 and Cu/Sb-0.41 in the 2 theta region 27–32° was done. The deconvoluted image shows the (111)/(410) and (020)/(301) planes related to CuSbS$_2$ phase very clearly (see the enlarged figure in the middle panel). Further lowering of the Sb precursor concentration in the bath, Cu/Sb-0.45, resulted in a decrease in the crystallinity of the samples despite the fact that there were characteristic CuSbS$_2$ peaks (Fig. 3d). Not all CuSbS$_2$ peaks were well defined for this film. With the sample Cu/Sb-0.45 it was not possible to carry out the deconvolution of the 2 theta region 27–32° because the peaks seem to be merged into a wide peak. XRD analysis evidenced that the sample Cu/Sb-0.41 showed better quality with no secondary phases. Raman analysis was further done to confirm this conclusion. To calculate crystallite size and lattice parameters of the CAS films the planes (200), (301), and (221) were used.

The microstructural data of the films are presented in Table 2. The lattice parameters were determined with the equation: $\frac{1}{d^2} = \frac{h^2}{a^2} + \frac{k^2}{b^2} + \frac{l^2}{c^2}$, where d represents the interplanar spacing and hkl corresponds to the miller indices of the plane. The average values obtained were a = 0.599 ± 0.01 nm, b = 0.379± 0.01 nm, and c = 1.464± 0.02 nm, which agrees with those reported in literature for CuSbS$_2$ [43]. The crystallite size was obtained using the Debye-Scherrer equation $D = \frac{0.9\lambda}{\beta_{hkl}\ cos\ \theta}$, where λ is the wavelength of Cukα(1.5406 Å), β_{hkl} is the full width at half maximum (FWHM), and θ is the Bragg angle. The highest crystallite size was obtained for the Cu/Sb-0.41 sample, ~19 nm, while the other two samples were close to 15–16 nm. The films developed from Cu/Sb-0.41 has a cell volume (332.35 Å) that is closer to strain-free orthorhombic CuSbS$_2$ powder (331.39 Å). This indicates a decrease in the lattice stress with the formation of stoichiometric CuSbS$_2$. The micro strain (ε) gives an impression of the compressive stress and local distortion and was calculated using the Scherrer relation, $\varepsilon = \frac{\beta}{4\ tan\ \theta}$. The lowest estimated strain was for Cu/Sb-0.41 sample which may be associated with its phase purity and its crystallinity. The dislocation density (δ) of the samples was determined by the equation $\delta = \frac{1}{D^2}$, and stoichiometric Cu/Sb-0.41 samples showed the lowest (Table 2). The preferential growth of crystals in an (hkl) plane was estimated from the texture coefficient (P_i), where N is the number of XRD peaks considered for analysis, ($I_{i(hkl)}$) and ($I_{io(hkl)}$) are the intensities of the (hkl) planes of the films and stress-free powder samples, respectively. If the values of P_i for a particular plane is greater than 1 those hkl planes are considered to have a preferential orientation. The P_i values of the (111) plane of the three samples were compared. The P_i of Cu/Sb-0.37, Cu/Sb-0.41 and Cu/Sb-0.45 were 1.00, 1.06 and 0.66, respectively. The standard variation (σ), which gives the degree of preferred orientation was obtained using the equation $\sigma = \sqrt{\frac{\sum_{i=1}^{N}(p_i - p_{io})^2}{N}}$, and $P_{io} = 1$ is the texture coefficient of stress-free sample. In general, for a randomly oriented sample σ is ≤ 0.6, and from the estimated values of σ for our samples, it can be noted that none of the samples showed preferred growth in any particular direction (Table 2).

Rietveld refinement of the XRD data was used to analyze the outcome of Cu/Sb precursor ratio on the formation of different phases

Table 3

Quantitative phase analysis, crystal size, lattice parameters and volume cell, of the electrodeposited CAS thin films obtained from the Rietveld refinement.

Sample	Molar ratio Cu/Sb	Weight % (wt.%)			Crystal size (nm)	Lattice parameters (nm)			Volume cell (Å^3)
		$CuSbS_2$	Sb_2S_3	$Cu_{12}SbS_{13}$		a	b	c	
Cu/Sb-0.37	0.37	78.31	21.69	–	19 ± 1	0.602	0.379	1.449	330.60
Cu/Sb-0.41	0.41	100	–	–	22 ± 2	0.603	0.380	1.449	332.20
Cu/Sb-0.45	0.45	74.26	15.70	10.04	17 ± 2	0.601	0.378	1.446	328.49
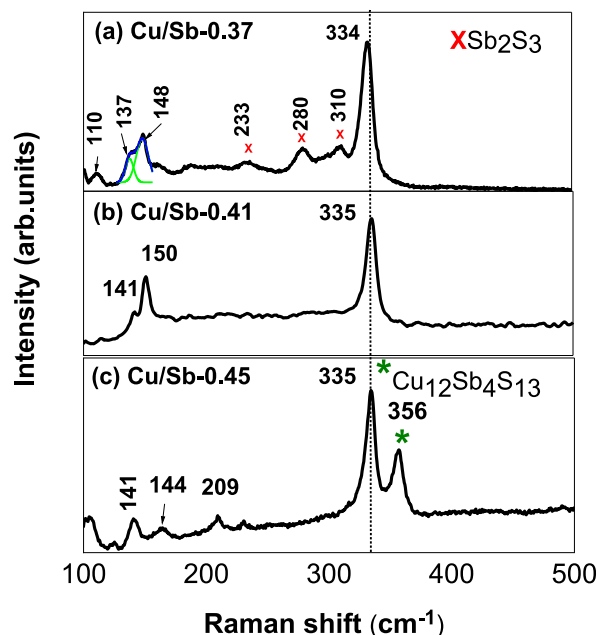
Fig. 4. Raman spectra of the CAS thin films pulse electrodeposited from baths with different precursor molar ratios. The Cu/Sb precursor ratios used for the deposition were 0.37, 0.41, 0.45.

in the films. The FullProf suite software was used for this purpose. Fig. 3f–h shows the experimental, calculated and difference profile of Rietveld refinement. The parameters deduced from the Rietveld refinement are shown in Table 3. The results of the Rietveld refinement indicate that the film developed at precursor molar ratios Cu/Sb = 0.37 and Cu/Sb = 0.45 are composed of different phases. The phase composition of the Cu/Sb-0.37 film was 78.31 % of $CuSbS_2$ and 21.69 % of Sb_2S_3, while that of Cu/Sb-0.45 had, in addition to $CuSbS_2$ (74.26 %), secondary phases such as Sb_2S_3(15.70 %) and $Cu_{12}Sb_4S_{13}$ (10.04 %). This confirmed that the Cu/Sb-0.41 film has stochiometric composition. The results of structural and quantitative phase analysis obtained from Rietveld refinement are presented in Table 3.

Raman analysis was done to identify the existence of any secondary phases which was not able to be determined in the XRD spectra and also to get information about the vibrational modes of the electrodeposited CAS thin films. The characteristic phononic vibrations of $CuSbS_2$ include both Raman and IR modes: A_g, B_{1g}, B_{2g}, and B_{3g} are Raman active and B_{1u}, B_{2u}, and B_{3u} are IR active modes [44]. Fig. 4a–c displays the Raman spectra of CAS deposited at distinct Cu/Sb precursor molar ratios. For all samples, there is a strong peak at 335 cm^{-1} which is the most intense peak reported for $CuSbS_2$ (A_g), attributed to the Sb–S stretching vibrational mode. The Raman spectra of Cu/Sb-0.37 shows peaks at 110, 137, 148, 233, 280, 310, and 334 cm^{-1}. Among these, the peaks at 110, 137, 148, and 334 cm^{-1} are related with the Raman modes of $CuSbS_2$ [45] whereas 233, 280, and 310 cm^{-1} correspond to that of Sb_2S_3 [46, 47]. The Raman peaks of the sample Cu/Sb-0.41 are at 141, 150, and 335 cm^{-1}. According to literature, these values agree well with the $CuSbS_2$ Raman modes. The absence of any other peaks demonstrates the phase purity of these samples. The Raman spectrum of the Cu/Sb-0.45 film shows the Raman peaks corresponding to both $CuSbS_2$ and tetrahedrite $Cu_{12}Sb_4S_{13}$ phases. The peaks at 141, 144, and 335 cm^{-1} correspond to $CuSbS_2$ [48] and that at 356 cm^{-1} to $Cu_{12}Sb_4S_{13}$ [49]. Therefore, the Raman results confirm that the sample Cu/Sb-0.41 have stoichiometric chalcostibite phase without any impurities. Further, the Raman spectroscopic results coincide with the conclusions from XRD analysis.

XPS analysis was done to explore the chemical state of the optimized electrodeposited film, Cu/Sb-0.41. In the survey scan, the peaks of Cu, Sb, S and C were observed (Fig. 5a). The adventitious carbon was used as reference. The high-resolution spectrum of Cu demonstrates two Gaussian peaks associated to Cu $2p_{1/2}$ and Cu $2p_{3/2}$ at binding energies (B.E) 952.0 and 932.2 eV, respectively (Fig. 5b). These B.E with peak separation 19.8 eV correspond to Cu$^+$ oxidation according to the literature. The absence of satellite
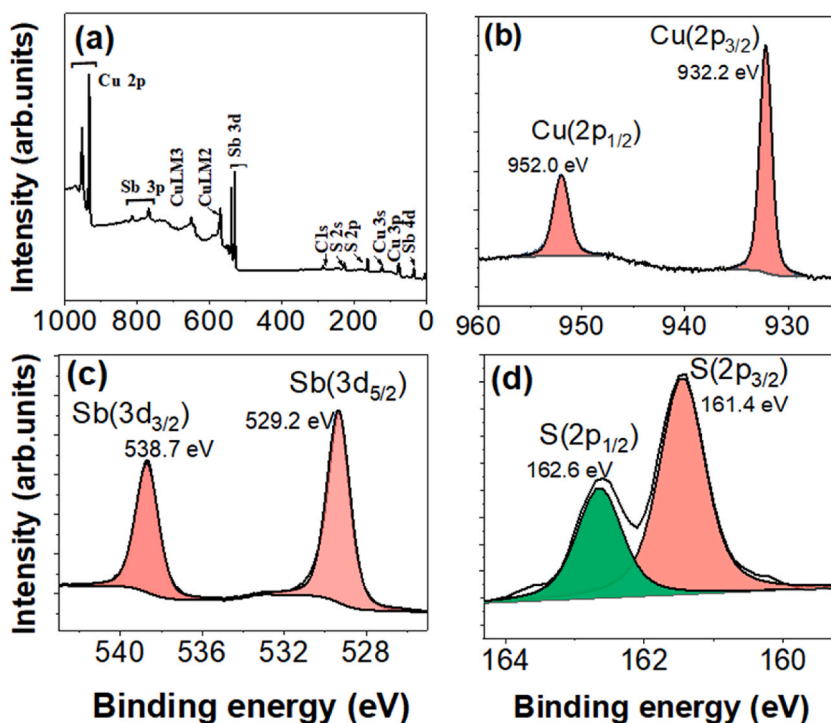
Fig. 5. XPS of the optimized CuSbS$_2$ (Cu/Sb-0.41) film (a) survey scan. Core level XPS spectra of (b) Cu 2p, (c) Sb 3d, (d) S 2p.
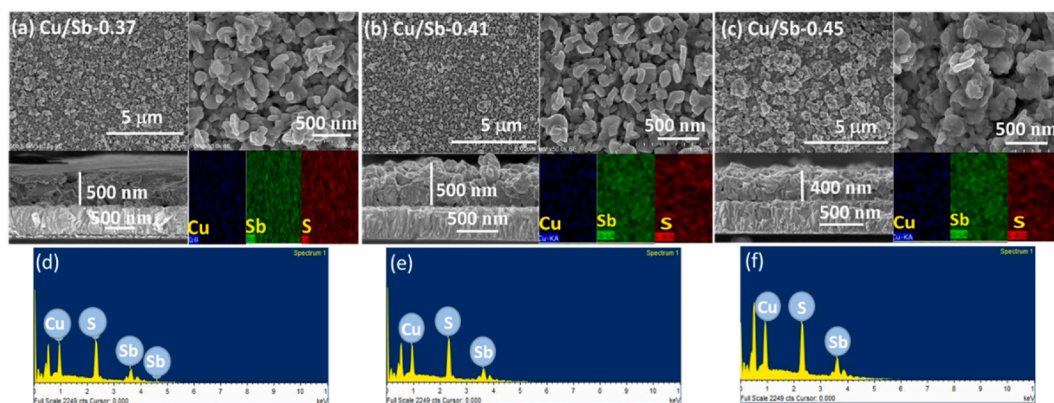

Fig. 6. (a–c). Surface and cross-sectional SEM images of CAS thin films electrodeposited at different Cu/Sb precursor ratio. EDS elemental mapping of these films are also included. (d–f) EDS spectrum of the CAS films.

peaks at ~936 and 942 eV confirmed that there are no Cu^{2+} in our samples. The antimony region showed the doublet at the binding energies at 538.7 eV (3d$_{3/2}$) and 529.2 eV (3d$_{5/2}$), which are consistent with Sb^{3+} (Fig. 5c) The XPS peaks at 162.6 and 161.4 eV with separation 1.2 eV and intensity ratio (2:1) is of S 2p$_{1/2}$ and 2p$_{3/2}$, respectively, which are congruent with the sulfide (S^{2-}) (Fig. 5d). Therefore, the XPS study confirms that the oxidation states of the elements in the films are (Cu$^+$) (Sb^{3+}) (S^{2-})$_2$, which are as expected for CuSbS$_2$ [48].

3.2. Morphological analysis

The surface topography of the CAS films was further evaluated through SEM images. The surface appearance of the samples, Cu/Sb-0.37 and Cu/Sb-0.41 (Fig. 6 a-b) were similar, whereas the films deposited at Cu/Sb-0.45 was distinct. The distribution of the grains is more uniform in the former films and the grains have an average size of ~100 nm. For Cu/Sb-0.45 films, the grains are seen to be more agglomerated (Fig. 6 c). The cross-sectional SEM images of the CAS thin films included along with the surface view show packed crystals. The interface between the FTO substrate and the films is very clear. The thicknesses of the CAS films are ~500 nm which is

Table 4

Composition analysis, wt. % and at. % of respective elements of CAS thin films obtained at different Cu/Sb precursor concentrations.

| Sample	Cu	wt.% Sb	S	Cu	at. % Sb	S	Cu/Sb at. %
Cu/Sb-0.37	21.9	57.4	20.3	23.8	32.5	43.7	0.73
Cu/Sb-0.41	25.2	49.1	24.2	25.5	25.9	48.6	0.98
Cu/Sb-0.45	32.0	46.3	25.3	30.1	22.7	47.2	1.32
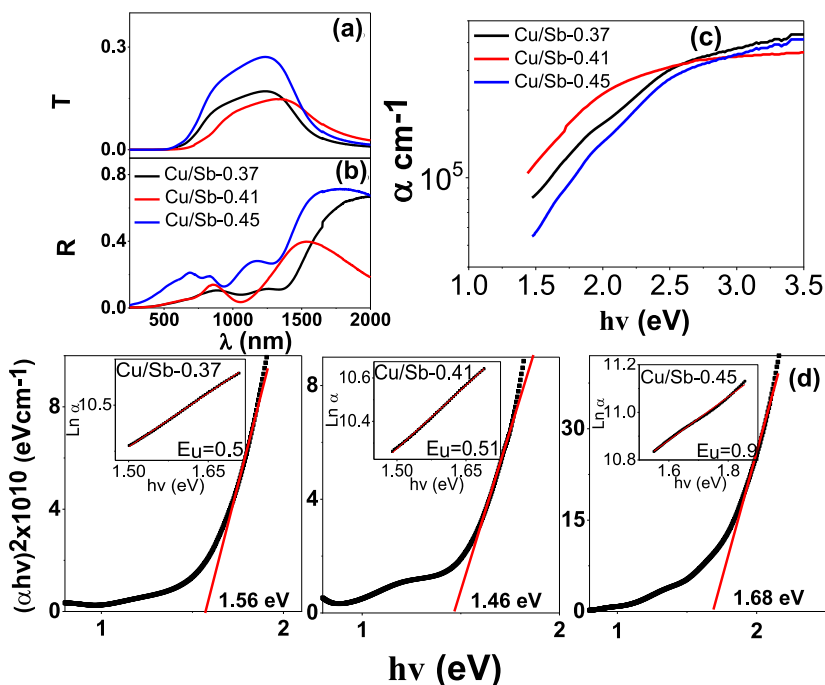
Fig. 7. a) Transmittance, and b) Reflectance spectra, c) Optical Absorption coefficient vs photon energy, (d) Tauc plot showing the band gap of the CAS thin films electrodeposited with different Cu/Sb precursor molar ratio. The inset shows Urbach energy.

consistent with that determined using surface profilometer. The elemental mapping of the samples included along with SEM images shows uniform spatial distribution of all the three elements, Sb, Cu, and S, in the films.

The atomic (at. %) and weight (wt. %) percent of the elements, Cu, Sb and S, estimated from the EDS measurements (Fig. 6(d–f)) and are given in Table 4. The Cu/Sb-0.37 film showed an excess of Sb and Cu/Sb-0.45 a high Cu content. The elemental composition of the CAS films was in accordance with the conclusions from XRD and Raman. The excess of Sb in Cu/Sb-0.37 and Cu in Cu/Sb-0.45 can be related to the presence of the secondary phases such as Sb_2S_3 and $Cu_{12}Sb_4S_{13,}$ respectively in those films. The film Cu/Sb-0.41 showed a stochiometric elemental composition (at.%) of Cu: Sb: S = 25.5 : 25.9: 48.6, which is very close to ideal composition of $CuSbS_2$. Apart from the SEM analysis the surface roughness and the morphology were analyzed using AFM images and the details are presented in the supplementary section (Fig. S3 a-c; section S2).

3.3. Optical analysis

Fig. 7 a-c presents the transmittance (T), reflectance (R) spectra and the calculated optical absorption coefficient (α) of Cu/Sb-0.37, Cu/Sb-0.41 and Cu/Sb-0.45 samples. The α was determined using the equation: $\alpha = \frac{1}{d} ln \left[\frac{(1-R)^2 + \sqrt{(1-R)^4 + (2RT)^2}}{2T} \right]$ [50], where d is the film thickness. The absorption coefficient of the samples in the visible region was in the range of 10^{-4} cm^{-1}. The relation between α and photon energy is given as $\alpha = \frac{A(hv - E_g)^n}{hv}$, where E_g is the energy gap, A is a constant, *h* is the Planck constant, *v* is the incident photon frequency and n is 2 for a direct band gap. From the linear region of Tauc plot (($\alpha hv)^2$ vs *hv*), a band gap of 1.56, 1.46 and 1.68 eV were estimated for the Cu/Sb-0.37, Cu/Sb-0.41, and Cu/Sb-0.45 samples, respectively (Fig. 7 d). The value of 1.56 eV obtained for the sample Cu/Sb-0.37 is in between the reported band gaps of stibnite and chalcostibite. These are consistent with XRD results showing stibnite and chalcostibite mixed phases (Fig. 3b). Cu/Sb-0.41 presents a band gap of 1.46 eV corresponding to pure chalcostibite, which is very near to E_g in literature [51,52]. However, for Cu/Sb-0.45 the E_g value estimated was 1.68 eV. This increase can be
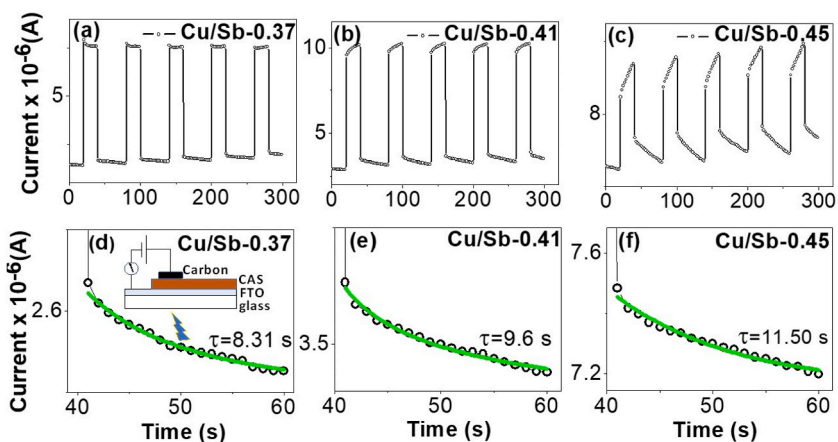
Fig. 8. (a–c) Transient photocurrent response of the films under an illumination intensity of 100 mW cm^{-2} and an applied voltage of 0.01 V. (d–f) Enlarged decay region of the photo response curves along with their exponential fittings. Inset shows the schematic representation of the sandwich configuration for the photo response measurement.
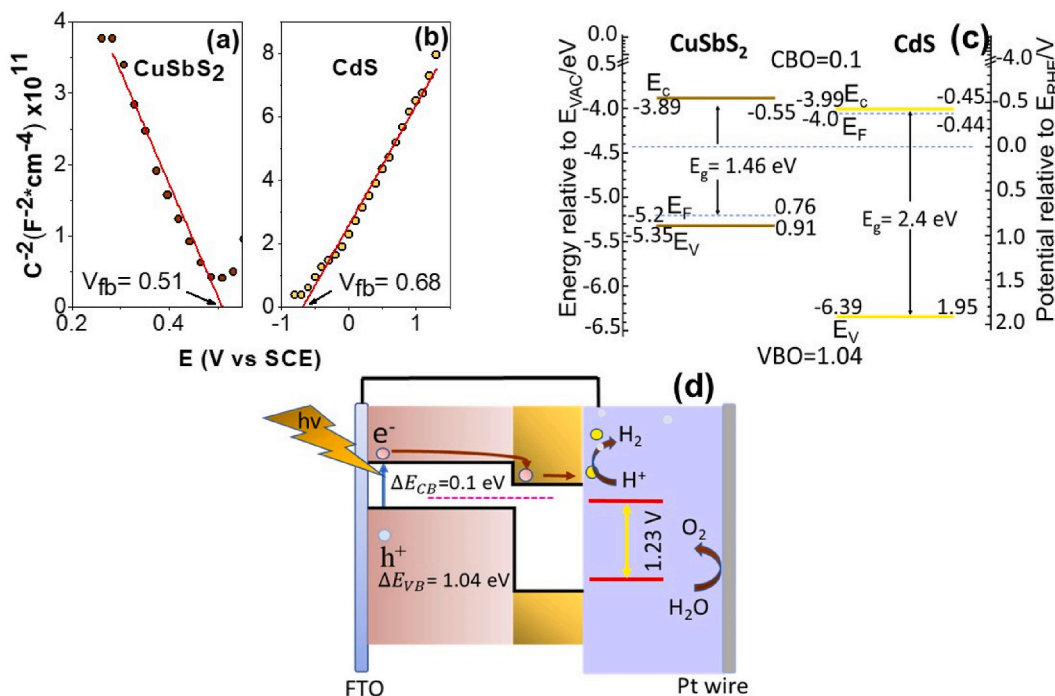
Fig. 9. Mott-Schottky plots of (a) p type CuSbS$_2$ and (b) n type CdS electrodes in 0.01 M H$_2$SO$_4$ solution under a frequency of 1 kHz, (c) Band energetic positions of CuSbS$_2$ and CdS with respect to RHE and vacuum (d) Schematic representation of the energy band alignment of CuSbS$_2$/CdS layers.

associated with the existence of tetrahedrite phase as revealed by Raman analysis. The E$_g$ of the tetrahedral phase Cu$_{12}$Sb$_4$S$_{13}$ is reported to be 1.83 eV [53]. The Urbach energies (E$_u$) of the samples, which can be related to the structural disorder and localized states within the E$_g$, was estimated from the graph $Ln\ \alpha = Ln\ \alpha_o + \frac{h\nu}{E_u}$ and is presented in the inset of Fig. 7d. The band tail width increased from 0.51 to 0.9 eV indicating an increase in the structural disorder for the film Cu/Sb-0.45 compared to other two films. The increase in E$_u$ may be attributed to the formation of the impurity tetrahedrite phase along with the chalcostibite.

3.4. Electrical properties

Fig. 8a–c shows the transient photocurrent response of the CAS thin films electrodeposited from baths with different Cu/Sb

Table 5
Dark and light conductivities, photosensitivity, and photocurrent decay of the CAS thin films.

	σ_d $(\Omega.cm)^{-1}$ x 10-5	σ_l $(\Omega.cm)^{-1}$ x 10-4	Sensitivity (%)	τ_1 (s)
Cu/Sb-0.37	7.75	4.00	417	8.31
Cu/Sb-0.41	14.80	5.06	243	9.60
Cu/Sb-0.45	30.20	4.21	39.2	11.50

Table 6
The electrical parameters of CuSbS$_2$ and CdS thin films obtained from Mott-Schottky plots.

	E_F (eV)	N_D (cm^{-3})	N_A (cm^{-3})	E_{CB}(eV)	E_{VB}(eV)
CuSbS$_2$	−5.2	–	7.27×10^{17}	−3.89	−5.35
CdS	−4.0	6.70×10^{18}	–	−3.99	−6.39

precursor molar ratio. Under an applied voltage of 0.01 V, the dark and light currents were measured. The intermittent dark and light conditions were employed by leaving the sample first for 20 s in dark, and then 20 s in illumination, and eventually 20 s in dark to complete the cycle. The intensity of the illumination was 100 mW cm^{-2}. Various dark/light cycles are shown to demonstrate the photostability of the films. The increase of current under light shows photosensitivity of the films. The dark conductivities of the samples Cu/Sb-0.37 and Cu/Sb-0.45 were 7.5×10^{-5} and 30.5×10^{-5} (ohm-cm)$^{-1}$, respectively. The observed rise in the conductivity is due to the high at. % of Cu in the Cu/Sb-0.45 films. The photosensitivity was calculated using the following equation: $S = \frac{(I_L - I_D)}{I_D}$, where I_L and I_D are the light and dark currents, respectively. The values obtained for Cu/Sb-0.37, Cu/Sb-0.41 and Cu/Sb-0.45 were 417, 243 and 39, respectively. The very low photosensitivity of the Cu/Sb-0.47 is due to the excess of Cu content in the films. The calculated light and dark conductivities and photosensitivity of the CAS thin films are presented in Table 5. As expected, an increase in the conductivity and a decrease in photosensitivity are observed with high copper content.

The enlarged photo response curves of the decay region of Cu/Sb-0.37, Cu/Sb-0.41 and Cu/Sb-0.45 are given in Fig. 8d–f. The transient decay curves were fitted to exponential equation, $I = I_0 + Ae^{-(t-t_0)/\tau}$, where I is the photocurrent at time t and I_o is the dark current, A is a constant, τ is transient decay time constant. The values of τ give an indication of the trap states in the material. Based on the curve fitting, decay time constants of samples were estimated: Cu/Sb-0.37 = 8.3 s, Cu/Sb-0.41 = 9.6 s, Cu/Sb-0.45 = 11.5 s. The fast decay process observed for the sample's Cu/Sb-0.37 and Cu/Sb-0.41, immediately after the light is off is due to the direct recombination of conduction band electrons and valence band holes. The slow transient decay shows the entrapment of photogenerated carriers in crystal defects, here the recombination process occurs through trap states collecting carriers that eventually return to the conduction band. The highest transient decay constant was for the Cu/Sb-0.45 indicating the presence of more trap states in those samples.

3.5. Photoelectrochemical measurements

The photoelectrochemical studies were done using the stoichiometric CuSbS$_2$ (Cu/Sb-0.41) sample. Fig. 9a–b shows the Mott-Schottky plots for CuSbS$_2$ and CdS obtained from the electrochemical impedance spectroscopy. The flat band potentials (E_{FB}) and conductivity types were determined using the equation,

$\frac{1}{C^2} = \frac{2}{\varepsilon_0 \varepsilon_s e A^2 N} \left(\pm E - E_{FB} - \frac{KT}{e} \right)$ here C is the space charge layer capacitance, ε_0 is the permittivity of vacuum (8.852×10^{-12} F/m), ε is the dielectric permittivity of the material (14.6), e is the charge of an electron (1.603×10^{-19} C),

N is the carrier concentration, k is Boltzman's constant (1.38×10^{-23} J/K), T is the temperature (300 K), E and E_{FB} are the applied and the flat band potentials, respectively. From the intercept and the slopes of the $1/C^2$ vs. potential plots (Fig. 9a–b), the E_{FB} and the carrier densities, respectively, were calculated. The E_{FB} and acceptor density (N_A) of the CuSbS$_2$ film were 0.51 V vs E_{RHE} and 7.27×10^{17} cm^{-3}. The E_{FB} and donor density (N_D) of CdS film were −0.68 eV and 6.7×10^{18} cm^{-3}, respectively. The positive and negative slopes of CuSbS$_2$ and CdS indicate their p-type and n-type conductivities. The effective density of states of the valence band (N_v) of CuSbS$_2$ and conduction band (N_c) of CdS were estimated using equations $N_V = 2 \left[\frac{2\pi m_h^* k_B T}{h^2} \right]^{\frac{3}{2}}$ and $N_c = 2 \left[\frac{2\pi m_e^* k_B T}{h^2} \right]^{\frac{3}{2}}$. In an electrochemical system the Fermi level of a semiconductor is equated to the E_{FB}. From values of E_{FB} and the density of the states of the bands, the valence position (E_{VB}) for p type CuSbS$_2$ and conduction position (E_{CB}) of n type CdS were calculated, $E_{VB} = E_F - k_B T ln \frac{N_V}{N_A}$,

$E_{CB} = E_F + k_B T ln \frac{N_c}{N_D}$. Subsequently, the valence/conduction band edges of the semiconductors were calculated from their respective band gap values. The energy level positions of E_F, E_{VB} and E_{CB} for CuSbS$_2$ and CdS with respect to E_{VAC} and E_{RHE} are shown in Fig. 9c and Table 6. For semiconductor photocatalysis, the positions of E_{CB} and Ev_B are important. The E_{CB} should be more negative than $E^o_{H+/H2}$ (0 V vs RHE), and E_{VB} more positive than $E^o_{O_2/H_2 O}$ (1.23 V vs RHE) at pH = 1. Using the values of the energy levels calculated, the band alignment of the CuSbS$_2$/CdS heterostructure is done and is shown in Fig. 9d. The conduction (ΔE_{CB}) and valence band (ΔE_{VB}) offset between the CuSbS$_2$/CdS heterostructure were 0.1 eV and 1.04 eV, respectively. This corresponds to a type II cliff like band structure where the Schottky junction formed between CuSbS$_2$/CdS promotes the charge separation reducing the recombination.
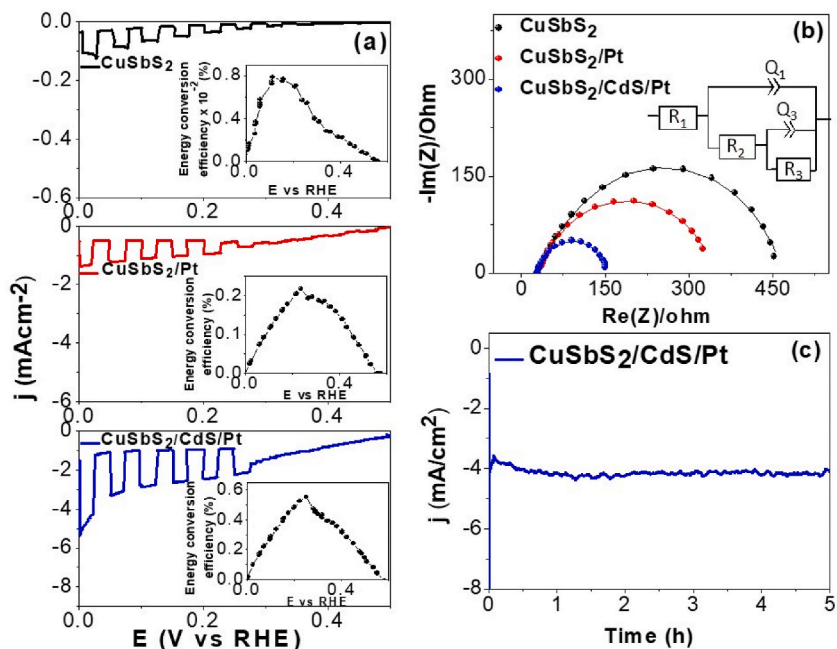
Fig. 10. a) Current density-potential curve (j-E) of CuSbS$_2$, CuSbS$_2$/Pt, CuSbS$_2$/CdS/Pt under pulsed light. The inset shows the energy conversion efficiency. (b) Nyquist plot of the CuSbS$_2$, CuSbS$_2$/Pt and CuSbS$_2$/CdS/Pt. The solid circles and continuous lines show the experimental and the fitted data, respectively. The equivalent circuit used for the EIS spectra is presented in the inset. c) Photo-stability of the CuSbS$_2$/CdS/Pt electrode in the PEC under 1 sun illumination.

Photoelectrochemical measurements were performed by lineal sweep voltammetry under pulsed light of 1 sun AM 1.5 G illumination. Fig. 10 shows the current density-potential curve (j-E) of the CuSbS$_2$, CuSbS$_2$/Pt and CuSbS$_2$/CdS/Pt photoelectrodes. The CuSbS$_2$ photoelectrode showed a low cathodic photocurrent response (0.07 mA cm^{-2} at 0 E$_{RHE}$) suggesting the need to include an additional layer that could boost the response. It has been demonstrated that Pt catalytic particles provide active sites for the improvement of the surface reactions [54]. For this, Pt nanoparticles were electrodeposited on CuSbS$_2$ surface. The details of the Pt deposition are given in the supplementary section (Sec. S3). The CuSbS$_2$/Pt photocathode exhibited improvement in the photocurrent, but still low photocurrent density (0.1 mA cm^{-2} at 0 E$_{RHE}$). Another strategy suggested is the use of CdS as a window layer, forming CuSbS$_2$/CdS heterostructure, which has been successfully tested with CZTS and GeSe absorber layers [55]. Here, ~70 nm of CdS was deposited between CuSbS$_2$ and Pt by chemical bath deposition to enhance the PEC performance. In CuSbS$_2$/CdS/Pt heterostructure photoelectrode, there was a significant increment in the photocurrent density (3.4 mA cm^{-2} at 0 E$_{RHE}$) which is related to the efficient charge separation by the electric field in the p-n heterojunction (CuSbS$_2$/CdS) and a reduction of surface recombination in an efficient way [55]. The photoconversion efficiency of the photocathodes was calculated with the equation Energy conversion efficiency = $\frac{|J| \times [E_{RHE} - E(H^+/H_2)]}{P} \times 100\%$, where E$_{RHE}$ is the applied potential vs RHE, E (H$^+$/H$_2$) correspond to the Nernst (equilibrium) potential for H$_2$ reaction (0 V vs RHE), j is the current density obtained (mA cm^{-2}) under light, and P is the incident power intensity (100 mW cm^{-2}). The efficiency increased from 0.008 % for CuSbS$_2$ to 0.56 % for CuSbS$_2$/CdS/Pt heterostructure at 0.25 E$_{RHE}$ (see inset Fig. 10 a-c).

The EIS analysis of the PEC was performed under short circuit conditions at 15 mV AC signal applied in a frequency range of 1 Hz–1 kHz. The measurements were fitted by the equivalent circuit showed in the inset of the Nyquist plot (fig. 10b and S4). It consists of R$_1$ that is the series resistance attributed to the contacts and wires, two capacitive elements (Q$_1$ and Q$_3$) and two resistive elements (R$_2$ and R$_3$). Q$_1$ corresponds to the capacitance of the space charge region, while Q$_3$ is related to the double-layer capacitance at the sample/electrolyte interface and are related to the defect states [56]. R$_2$ and R$_3$ are the resistance corresponding to the trapping/detrapping of electrons within states in the band gap and the charge transport, respectively [57]. The Nyquist plot of the CuSbS$_2$, CuSbS$_2$/Pt and CuSbS$_2$/CdS/Pt samples are presented in Fig. 10b. A decrement of the radius of semicircle arc was observed, which indicates that the incorporation of Pt and CdS in the CuSbS$_2$ photocathode promoted a significant reduction of the charge transport resistance (R$_3$) compared to the CuSbS$_2$ photocathode alone. This decrease of R$_3$ lead to an improvement in photoelectrochemical activity. Furthermore, the R$_2$ decreased considerably when CdS was added associated to the formation of CuSbS$_2$/CdS heterostructure. It agrees with the effect of the energy levels alignment (Fig. 9c–d), where the CdS/CuSbS$_2$ form a type II band structure, enhancing charge separation and reducing the e$^-$/h$^+$ recombination at the semiconductor electrolyte interface. This led to a faster charge transport at the interface and an increment of the efficiency of the PEC.

Both capacitances (Q$_1$ and Q$_3$) were reduced when Pt and CdS were incorporated into CuSbS$_2$ to form the photocathode structure. The reduction of Q$_1$ and Q$_3$ could be related to the decrease of defect states at the bulk and electrode/electrolyte interface. The values of capacitances and resistances calculated are given in Table 7. Otherwise, these defects would have become recombination centers for

Table 7
The series resistance attributed to the contacts (R_1), the resistance corresponding to the trapping/detrapping of electrons within states in the band gap and the charge transport R_2 and R_3 respectively of $CuSbS_2$, $CuSbS_2$/Pt, $CuSbS_2$/CdS/Pt.

	R_1 (Ω)	R_2 (Ω)	R_3 (Ω)	Q_1 10^{-3} (F)	Q_3 10^{-6} (F)
$CuSbS_2$	31.62	258	176	20.5	660
$CuSbS_2$/Pt	31.85	250	63	0.1	10.6
$CuSbS_2$/CdS/Pt	33.01	79	36	0.1	9.2

photogenerated carriers [23,56]. Additionally, Fig. 10c shows the stability of the photocathode in the PEC, where it can be observed that the photocurrent of $CuSbS_2$/CdS/Pt structure remained stable for 5 h under illumination, which is a promising behavior for the photoelectrochemical application.

4. Conclusions

Here in, we detail the development of stoichiometric $CuSbS_2$ thin films on FTO substrates via pulse potential electrodeposition technique. The optimized pulse potentials applied for the deposition of the films were V_{on} −0.72 V and V_{off} −0.1 V vs SCE at 50 % duty cycle. The influence of Cu/Sb precursor molar ratio on the phase formation was studied. A compact and stochiometric $CuSbS_2$ thin films was obtained with a precursor ratio Cu/Sb = 0.41. These $CuSbS_2$ films were tested as photocathodes in a photoelectrochemical cell. The formation of the p-n heterostructure, CdS/$CuSbS_2$, significantly improved the photocurrent. The heterojunction formed showed a cliff like structure which contributed to reduction of recombination and improved charge separation. The Pt catalyst deposited further improved the charge transfer in the photoelectrode/electrolyte interface. The obtained photocurrent density of $CuSbS_2$/CdS/Pt was 3.4 mA cm^{-2} at 0 V vs RHE. The photocurrent was stable for 5 h under illumination showing the stability of the photocathode for the application of H_2 production. In summary, we demonstrate the development of thin films of $CuSbS_2$, a photo-cathode with earth-abundant constituent elements, by a low-cost technique and its application in the cost-effective evolution of hydrogen.

CRediT authorship contribution statement

R.G. Avilez García: Writing – original draft, Methodology, Investigation, Formal analysis. **Andrea Cerdán-Pasarán:** Writing – review & editing, Formal analysis, Data curation. **J.P. Enríquez:** Formal analysis. **N.R. Mathews:** Writing – review & editing, Investigation, Funding acquisition, Formal analysis, Data curation, Conceptualization.

Declaration of competing interest

The authors declare that they have no known competing financial interests or personal relationships that could have appeared to influence the work reported in this paper.

Acknowledgments

Appendix A. Supplementary data

Supplementary data to this article can be found online at https://doi.org/10.1016/j.heliyon.2024.e24491.
Data will be made available on request.

References

[1] L. Claudio Andreani, A. Bozzola, P. Kowalczewski, M. Liscidini, L. Redorcii, Silicon solar cells: toward the efficiency limits, Adv. Phys.: x 4 (2019) 1548305, https://doi.org/10.1080/23746149.2018.1548305.
[2] Ran Chen, Matthew Wright, Daniel Chen, Jie Yang, Peiting Zheng, Xinyu Zhang, Wenham Stuart, Alison Ciesla, 24.58% efficient commercial n-type silicon solar cells with hydrogenation, Prog Photovolt Res Appl 29 (2021) 1213–1218.
[3] Michael Powalla, Stefan Paetel, Dimitrios Hariskos, Wuerz Roland, Friedrich Kessler, Peter Lechner, Wiltraud Wischmann, Theresa Magorian Friedlmeier, Advances in cost-efficient thin-film photovoltaics based on Cu(in,Ga)Se$_2$, Engineering 3 (4) (2017) 445–451, https://doi.org/10.1016/J.ENG.2017.04.015.
[4] Alessandro Romeo, Elisa Artegiani, CdTe-based thin film solar cells: past, Present and Future 14 (2021) 1684, https://doi.org/10.3390/en14061684.
[5] A. Fujishima, K. Honda, Electrochemical Photolysis of water at a semiconductor electrode, Nature 238 (1972) 37–38, https://doi.org/10.1038/238037a0.

[6] Kot Anna, DominiK. Dorosz, Marta Radecka, Katarzyna Zakrzewska, Improved photon management in a photoelectrochemical cell with Nd-modified TiO₂ thin film photoanode, Int. J. Hydrogen Energy 46 (22) (2021) 12082–12094, https://doi.org/10.1016/j.ijhydene.2020.05.094.

[7] Joaquin Resasco, Hao Zhang, Nikolay Kornienko, Nigel Becknell, Hyunbok Lee, Jinghua Guo, Alejandro L. Briseno, Peidong Yang, TiO₂/BiVO₄ nanowire heterostructure photoanodes based on type II band alignment, ACS Cent. Sci. 2 (2016) 80–88, https://doi.org/10.1021/acscentsci.5b00402.

[8] Sizhuo Guo, Xin Zhao, Weiwei Zhang, Wenzhong Wang, Optimization of electrolyte to significantly improve photoelectrochemical water splitting performance of ZnO nanowire arrays, Mater. Sci. Eng., B 227 (2018) 129–135, https://doi.org/10.1016/j.mseb.2017.09.020.

[9] Lichao Jia, Karsten Harbauer, Bogdanoff Peter, Iris Herrmann-Geppert, Alejandra Ramírez, Roel van de Krol, Sebastian Fiechter, α-Fe2O3 films for photoelectrochemical water oxidation – insights of key performance parameters, J. Mater. Chem. A 2 (47) (2014) 20196–20202, https://doi.org/10.1039/C4TA04720F.

[10] Kai-Hang Ye, Haibo Li, Duan Huang, Shuang Xiao, Weitao Qiu, Mingyang Li, Yuwen Hu, Wenjie Mai, Hongbing Ji, Shihe Yang, Enhancing photoelectrochemical water splitting by combining work function tuning and heterojunction engineering, Nat. Commun. 10 (2019) 3687, https://doi.org/10.1038/s41467-019-11586-y.

[11] Morteza Kolaei, Meysam Tayebi, Zohreh Masoumi, Tayyebi Ahmad, Byeong-Kyu Lee, Decoration of CdS nanoparticles on dense and multi-edge sodium titanate nanorods to form a highly efficient and stable photoanode with great enhancement in PEC performance, Environ. Sci.: Nano 8 (2021) 1667, https://doi.org/10.1039/d1en00221j.

[12] T. Jesper Jacobsson, Viktor Fjällström, Marika Edoff, Tomas Edvinsson, CIGS based devices for solar hydrogen production spanning from PEC-cells to PV-electrolyzers: a comparison of efficiency, stability and device topology, Sol. Energy Mater. Sol. Cell. 134 (2015) 185–193, https://doi.org/10.1016/j.solmat.2014.11.041.

[13] Wooseok Yang, Yunjung Oh, Jimin Kim, Myung Jin Jeong, Jong Hyeok Park, Jooho Moon, Molecular chemistry-controlled hybrid ink derived efficient Cu₂ZnSnS₄ photocathodes for photoelectrochemical water splitting, ACS Energy Lett. 1 (2016) 1127–1136, https://doi.org/10.1021/acsenergylett.6b00453.

[14] Dingwang Huang, Lintao Li, Kang Wang, Yan Li, Feng Kuang, Feng Jiang, Wittichenite semiconductor of Cu₃BiS₃ films for efficient hydrogen evolution from solar driven photoelectrochemical water splitting, Nat. Commun. 12 (2021) 3795, https://doi.org/10.1038/s41467-021-24060-5.

[15] H.D. Shelke, A.C. Lokhande, J.H. Kim, C.D. Lokhande, Photoelectrochemical (PEC) studies on Cu₂SnS₃ (CTS) thin films deposited by chemical bath deposition method, J. Colloid Interface Sci. 506 (2017) 144–153, https://doi.org/10.1016/j.jcis.2017.07.032.

[16] Yanbo Li Zhang, Li Xiao Li, Changli Li, Rujing Zhang, Jean-Jacques Delaunay, Hongwei Zhu, Solution-processed CuSbS₂ thin film: a promising earth-abundant photocathode for efficient visible-light-driven hydrogen evolution, Nano Energy 28 (2016) 135–142, https://doi.org/10.1016/j.nanoen.2016.08.036.

[17] M. Oubakalla, M. Bouachri, M. Beraich, M. Taibi, A. Guenbour, A. Bellaouchou, F. Bentiss, A. Zarrouk, M. Fahoume, The properties of the Cu3SbS3 thin film Co-electrodeposited on the FTO enriched with the DFT-calculation, Chemistry Africa 39 (2022), https://doi.org/10.1007/s42250-022-00507-0.

[18] Bo Yang, Liang Wang, Jun Han, Ying Zhou, Huaibing Song, Shiyou Chen, Jie Zhong, Lv Lu, Dongmei Niu, Tang Jiang, CuSbS₂ as a promising earth-abundant photovoltaic absorber material: a combined theoretical and experimental study, Chem. Mater. 16 (2014) 3135–3143, https://doi.org/10.1021/cm500516v.

[19] Shahara Banu, Se Jin Ahn, Seung Kyu Ahn, Kyunghoon Yoon, Ara Cho, Fabrication and characterization of cost-efficient CuSbS₂ thin film solar cells using hybrid inks, Sol. Energy Mater. Sol. Cells 151 (2016) 14–23, https://doi.org/10.1016/j.solmat.2016.02.013.

[20] Lijuan Fu, Junsheng Yu, Jinsong Wang, Xie Fan, Shun Yao, Yongsong Zhang, Cheng Jiang, Li Lu, Thin film solar cells based on Ag-substituted CuSbS₂ absorber, Chem. Eng. J. 400 (2020) 125906, https://doi.org/10.1016/j.cej.2020.125906.

[21] Seger Brian, Ivano E. Castelli, Peter C.K. Vesborg, Karsten W. Jacobsen, Ole Hansenand, Ib Chorkendorff, 2-Photon tandem device for water splitting: comparing photocathode first versus photoanode first designs, Energy Environ. Sci. 7 (8) (2014) 2397–2413, https://doi.org/10.1039/C4EE01335B.

[22] Peidong Wu, Zhifeng Liu, Mengnan Ruan, Zhengang Guo, Lei Zha, Cobalt-phosphate modified Fe-Zn₀.₂Cd₀.₈S/CuSbS₂ heterojunction photoanode with multiple synergistic effect for enhancing photoelectrochemical water splitting, Appl. Surf. Sci. 476 (2019) 716–723, https://doi.org/10.1016/j.apsusc.2019.01.150.

[23] Shiwei Wang, Zhengyang Zhang, Yanjun Wang, Minmin Han, Hierarchical hollow CuSbS₂ microspheres with excellent photoelectrochemical properties, Mater. Lett. 12 (2021) 100094, https://doi.org/10.1016/j.mlblux.2021.100094.

[24] Qianyuan Chen, Zhongchi Wang, Keqiang Chen, Qiang Fu, Yueli Liu, Yupeng Zhang, Delong Li, Chunxu Pan, TiO₂/graphene/CuSbS₂ mixed-dimensional array with high-performance photoelectrochemical properties, RSC Adv. 9 (58) (2019) 33747–33754, https://doi.org/10.1039/c9ra07237c.

[25] Y. Zhang, J. Huang, C. Yan, K. Sun, X. Cui, F. Liu, Z. Liu, X. Zhang, X. Liu, J.A. Stride, M.A. Green, High open-circuit voltage CuSbS₂ solar cells achieved through the formation of epitaxial growth of CdS/CuSbS₂ hetero-interface by post annealing treatment, Prog. Photovoltaics Res. Appl. 27 (2018) 37–43, https://doi.org/10.1002/pip.3061.

[26] L. Wan, C. Ma, K. Hu, R. Zhou, X. Mao, S. Pan, L. Helena, J. Xu, Two-stage coevaporated CuSbS₂ thin films for solar cells, J. Alloys Compd. 680 (2016) 182–190, https://doi.org/10.1016/j.jallcom.2016.04.193.

[27] F.E. Loranca-Ramos, C.J. Diliegros-Godines, R. Silva González, Mou Pal, Structural, optical and electrical properties of copper antimony sulfide thin films grown by a citrate-assisted single chemical bath deposition, Appl. Surf. Sci. 427 (2018) 1099–1106, https://doi.org/10.1016/j.apsusc.2017.08.027.

[28] Wilman Septina, Shigeru Ikeda, Iga Yuta, Takashi Harada, Michio Matsumura, Thin film solar cell based on CuSbS₂ absorber fabricated from an electrochemically deposited metal stack, Thin Solid Films 550 (2014) 700–704, https://doi.org/10.1016/j.tsf.2013.11.046.

[29] Lei Wan, Xu Guo, Yingcui Fang, Xiaoli Mao, Huier Guo, Jinzhang Xu, Ru Zhou, Spray pyrolysis deposited CuSbS₂ absorber layers for thin-film solar cells, J. Mater. Sci. Mater. Electron. 30 (2019) 21485–21494, https://doi.org/10.1007/s10854-019-02531-2.

[30] Joel van Embden, Joao O. Mendes, Jacek J. Jasieniak, Anthony S.R. Chesman, Enrico Della Gaspera, Solution-processed CuSbS₂ thin films and superstrate solar cells with CdS/In₂S₃ buffer layers, ACS Appl. Energy Mater. 3 (8) (2020) 7885–7895, https://doi.org/10.1021/acsaem.0c01296.

[31] M. Oubakalla, M. Beraich, M. Taibi, H. Majdoubi, Y. Aichi, A. Guenbour, A. Bellaouchou, F. Bentiss, A. Zarrouk, M. Fahoume, The choice of the copper concentration favoring the production of stoichiometric CuSbS₂ and Cu₁₂Sb₄S₁₃ thin films co-electrodeposited on FTO, J. Alloys Compd. 908 (2022) 164618, https://doi.org/10.1016/j.jallcom.2022.164618.

[32] R.N. Bhattacharya, W. Batchelor, Thin film CuIn₁₋ₓGaₓSe2CuIn₁₋ₓGaₓSe photovoltaic cells from solution-based precursor layers, Appl. Phys. Lett. 75 (1999) 1431, https://doi.org/10.1063/1.124716.

[33] Jonathan J. Scragg, M. Dominik, Berg, J. Phillip, A.3 Dale, 2% efficient Kesterite device from electrodeposited stacked elemental layers, J. Electroanal. Chem. 646 (1–2) (2010) 52–59, https://doi.org/10.1016/j.jelechem.2010.01.008.

[34] K.V. Gurav, J.H. Yunb, S.M. Pawara, S.W. Shina, M.P. Suryawanshia, Y.K. Kima, G.L. Agawanea, P.S. Patila, J.H. Kima, Pulsed electrodeposited CZTS thin films: effect of duty cycle, Mater. Lett. 108 (2013) 316–319, https://doi.org/10.1016/j.matlet.2013.06.062.

[35] U. Chalapathi, B. Poornaprakash, C.H. Ahn, S.H. Park, Two-stage processed CuSbS2 thin films for photovoltaics: effect of Cu/Sb ratio, Ceram. Int. 44 (12) (2018), https://doi.org/10.1016/j.ceramint.2018.05.117.

[36] R.G. Sotelo Marquina, T.G. Sanchez, E. Regalado-Perez, J. Pantoja-Enriquez, N.R. Mathews, Omar S. Martinez, X. Mathew, CuSbS2 thin films by heat treatment of thermally evaporated Sb2S3/CuS stack: Effect of [Cu]/[Sb] ratio on the physical properties of the films 204 (2022) 111355, https://doi.org/10.1016/j.vacuum.2022.111355.

[37] Masih Soleymani, Farzaneh Sadri, Susanna Zhang, Ghahreman Ahmad, The role of thiosulfate and sulfite in gold thiosulfate electrowinning process: an electrochemical view, Process Saf. Environ. Protect. 166 (2022) 232–240, https://doi.org/10.1016/j.psep.2022.08.028.

[38] Venko Beschkov, Elena Razkazova-Velkova, Martin Martinov, Stefan Stefanov, Electricity production from marine water by sulfide-driven fuel cell, Appl. Sci. 8 (2018) 1926. https://doi:10.3390/app8101926.

[39] A.J. Bard, B. Parsons, J. Jordan, in: G. Milazzo, S. Caroli, V.K. Sharma (Eds.), Standard Potentials in Aqueous Solutions, Dekker: New York, Tables of Standard Electrode Potentials, Wiley, London, 1985, 1978.

[40] A.J. Bard, L.R. Faulkner, C.G. Zoski, Electrochemical Methods: Fundamentals and Applications, Wiley, New York, 1980.

[41] José A. Zamora Zeledón, Ariel Jackson, Michaela Burke Stevens, Gaurav A. Kamat, Thomas F. Jaramillo, Methods-A practical approach to the reversible hydrogen electrode scale, J. Electrochem. Soc. 169 (2022) 066505, https://doi.org/10.1149/1945-7111/ac71d1.

[42] N. R. Janardhana Rastogi, Properties of CuSbS$_2$ thin films electrodeposited from ionic liquids as p-type absorber for photovoltaic solar cells, Thin Solid Films 565 (2014), https://doi.org/10.1016/j.tsf.2014.06.031.

[43] Abdelaziz Gassoumi, H.-E. Mohamed Musa Saad, Salem Alfaify, Tarek Ben Nasr, Nadir Bouarissa, The investigation of crystal structure, elastic and optoelectronic properties of CuSbS$_2$ and CuBiS$_2$ compounds for photovoltaic applications 725 (2017) 181–189, https://doi.org/10.1016/j.jallcom.2017.07.141.

[44] Jason Baker, Ravhi S. Kumar, Daniel Sneed, Anthony Connolly, Yi Zhang, Nenad Velisavljevic, Jayalakshmi Paladugu, Michael Pravica, Changfeng Chen, Andrew Cornelius, Yusheng Zhao, Pressure induced structural transitions in CuSbS$_2$ and CuSbSe$_2$ thermoelectric compounds, J. Alloys Compd. 643 (2015) 186–194, https://doi.org/10.1016/j.jallcom.2015.04.138.

[45] S. Vinayakumar, Shaji, D. Avellaneda, J.A. Aguilar-Martínez, B. Krishnan, Copper antimony sulfide thin films for visible to near infrared photodetector applications, RSC Adv. 8 (2018) 31055–31065, https://doi.org/10.1039/C8RA05662E.

[46] Qi Wang, Fangyang Liu, Li Wang, Liangxing Jiang, Qiyu Wang, Bo Hong, Yanqing Lai, Towards fast and low cost Sb$_2$S$_3$ anode preparation: a simple vapor transport deposition process by directly using antimony sulfide ore as raw material, Scripta Mater. 173 (2019) 75–79, https://doi.org/10.1016/j.scriptamat.2019.07.032.

[47] Sherif Kharbishi, Eugen Libowitzky, Anton Beran, Raman spectra of isolated and interconnected pyramidal XS$_3$ groups (X = Sb, Bi) in stibnite, bismuthinite, kermesite, stephanite and bournonite, European Journal Mineral 21 (2) (2009) 325–333, https://doi.org/10.1127/0935-1221/2009/0021-1914.

[48] L. Wan, C. Ma, K. Hu, R. Zhou, X. Mao, S. Pan, L. Helena, J. Xu, Two-stage coevaporated CuSbS$_2$ thin films for solar cells, J. Alloys Compd. 680 (2016) 182–190, https://doi.org/10.1016/j.jallcom.2016.04.193.

[49] Thomas Rath, J. Andrew, Mac Lachlan, Michael D. Brown, Saif A. Haque, Structural, optical and charge generation properties of chalcostibite and tetrahedrite copper antimony sulfide thin films prepared from metal xanthates, J. Mater. Chem. A 3 (47) (2015) 24155, https://doi.org/10.1039/C5TA05777A.

[50] Optical Processes in Semiconductors, Pankov, Jacques I., Prentice-Hall, Dover publications, 1971.

[51] S. Manolache, A. Duta, L. Isac, M. Nanu, A. Goossens, J. Schoonman, The influence of the precursor concentration on CuSbS$_2$ thin films deposited from aqueous solutions, Thin Solid Films 515 (15) (2007) 5957–5960, https://doi.org/10.1016/j.tsf.2006.12.046.

[52] Koji Takei, Tsuyoshi Maeda, Takahiro Wada, Crystallographic and optical properties of CuSbS$_2$ and CuSb(S$_{1-x}$Se$_x$)$_2$ solid solution, Thin Solid Films 582 (2015) 263–268, https://doi.org/10.1016/j.tsf.2014.11.029.

[53] Muthusamy Tamilselvan, Aninda, J. Bhattacharyya, Tetrahedrite (Cu$_{12}$Sb$_4$S$_{13}$) ternary inorganic hole conductor for ambient processed stable perovskite solar cells, ACS Appl. Energy Mater. 1 (8) (2018) 4227–4234, https://doi.org/10.1021/acsaem.8b00844.

[54] Yasemin Aykut, Ayşe Bayrakçeken Yurtcan, the role of the Pd ratio in increasing the activity of Pt for high efficient hydrogen evolution reaction, J. Electroanal. Chem. 921 (2022) 116711, https://doi.org/10.1016/j.jelechem.2022.116711.

[55] Dingwang Huang, Lintao Li, Kang Wang, Yan Li, Feng Kuang, Feng Jiang, Wittichenite semiconductor of Cu$_3$BiS$_3$ films for efficient hydrogen evolution from solar driven photoelectrochemical water splitting, Nat. Commun. 12 (2021) 3795.

[56] R. C. Bredar Alexandria, Amanda L. Chown, Andricus R. Burton, Byron H. Farnum, Electrochemical impedance spectroscopy of metal oxide electrodes for energy applications, ACS Appl. Energy Mater. 3 (1) (2020) 66–98, https://doi.org/10.1021/acsaem.9b01965.

[57] Jiheng Zhao, Yu Guo, Lili Cai, Li Hong, Ken Xingze Wang, Cho In Sun, Chi Hwan Lee, Shanhui Fan, Xiaolin Zheng, High-Performance ultrathin BiVO$_4$ photoanode on textured polydimethylsiloxane substrates for, Solar Water Splitting 1 (1) (2016) 68–75, https://doi.org/10.1021/acsenergylett.6b00032.